

Supplementary Information

Wearable energy storage with MXene textile supercapacitors for real world use

Alex Inman ^{1,#}, Tetiana Hryhorchuk ^{1,#}, Lingyi Bi ^{1,2}, Ruocun (John) Wang ¹, Ben Greenspan ³, Taylor Tabb ³, Eric M. Gallo ³, Armin VahidMohammadi ¹, Genevieve Dion ², Andreea Danielescu ^{3,*}, Yury Gogotsi ^{1,*}

These authors have contributed equally to this work, * Corresponding authors:

Andreea Danielescu andreea.danielescu@accenture.com; Yury Gogotsi gogotsi@drexel.edu

¹ *A.J. Drexel Nanomaterials Institute and Department of Material Science and Engineering, Drexel University, 3141 Chestnut St., Philadelphia, PA 19104, United States*

² *Center for Functional Fabrics, Drexel University, 3141 Chestnut St., Philadelphia, PA 19104, United States*

³ *Accenture Labs, 415 Mission St. Fl. 34, San Francisco, CA 94105, United States*

Table S1 – Wearable supercapacitors State-of-the-art

Electrodes	Possible power applications	E (mWh cm ⁻²)	C (mF cm ⁻²)	Voltage (V)	Ref.
Ti₃C₂T_x MXene-cotton	Programmable microelectronics	0.401	146	6/5	This work
ACFC-PANI-CNTs-MnO ₂ //ACFC	LED	0.413	2606	1.5	1
ONCT//MNCT	Digital watch	0.277	780	1.6	2
Single layer cotton	--	0.205	49	1.5	3
NiCo ₂ S ₄ -CNT//MXene-CCT	LED	0.174	559	1.5	4
Lig-PANI-FGH-FCC	--	0.170	1233	1	5
BMX//BRU	Digital watch	0.168	554	1.5	6
PANI//MXene	Digital watch	0.159	585	1.4	7
Co ₉ S ₈ -PPy-NiCo-LDH-NTAs//AC	LED	0.132	371	1.6	8
MXene aerogel//ESCNF	LED	0.120	532	1.3	9
rGO-CNT//NiCo-BOH	Digital watch	0.078	80	1.4	10
Activated carbon fabrics	--	0.077	554	1	11
PPy-rGO-M-PEFY	LED	0.066	350	1	12
Graphene-PANI	Display	0.063	708	0.8	13
PANI-RGO-PMFT	Fan	0.050	564	0.8	14
Cu(OH) ₂ -CPCC//AC-CC	LED	0.049	243	1.2	15
Ppy-WCF	Digital watch	0.041	456	0.8	16
RuO ₂ //MXene	LED	0.037	60	1.5	17
PANI-CNT-textile	LED	0.037	412	0.8	18
CWF-PANI-RGO	LED	0.028	198	1	19
rGOFF-PANI	LED	0.028	816	1	20
MXene-MPFs	Watch	0.020	408	0.6	21
PET-rGO-PPY	--	0.011	230	1	22
EG-PEDOT:PSS-MWCNT-RGO	Digital watch	0.005	30	1.0	23
MXene-MSC	--	0.004	71	0.6	24
CF-MoO ₃ //CF-MnO ₂	LED	0.003	5	2	25
TiN-C nanotubes-fiber	LED	0.003	19	1	26
3D MSC	Photodetector	0.001	35	0.6	27
PET-MXene	LED	0.001	18	0.6	28
ERGO-Ni-Cotton	LED	0.0003	5	0.8	29
MXene//SWCNT	PVA/H ₂ SO ₄	0.0001	1	1.0	30

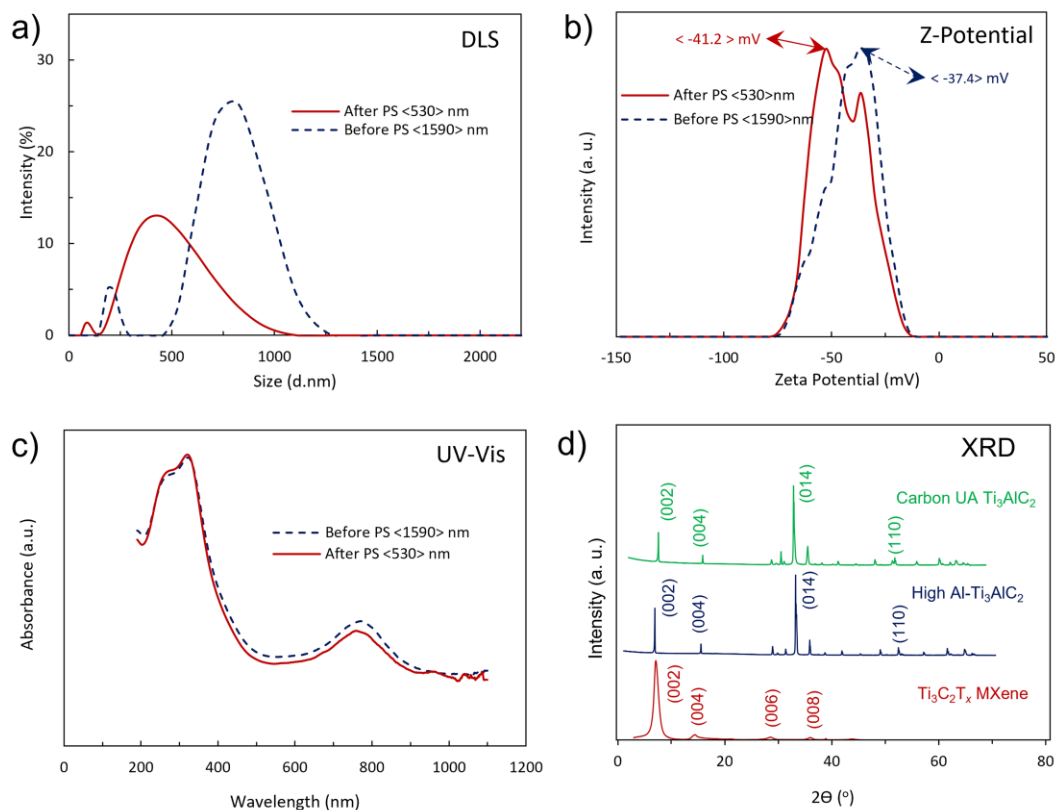


Figure S1 – DLS (a), Z-Potential (b), UV-Vis (c), XRD data (d) on $\text{Ti}_3\text{C}_2\text{T}_x$ MXene

Table S2 – Data on loading, footprint area and samples resistivity

A (cm^2)	$\text{Ti}_3\text{C}_2\text{T}_x$ (mg cm^{-2})	R(Ω) per 11 cm	Charging method	Discharge I (mA cm^{-2})	Discharge t (min)	Q (mA.h)	C (mF cm^{-2})	E (mWh cm^{-2})	P (mW cm^{-2})
CV									
25	24.2	2	60 min	0.16	97	6.07	146	0.401	0.248

Table S3 – Data on varying footprint area samples used for testing within this work

Footprint (cm^2)	Active $\text{Ti}_3\text{C}_2\text{T}_x$ loading (g)	$\text{Ti}_3\text{C}_2\text{T}_x$ loading (mg cm^{-2})	Resistivity
4	0.156	3.9	10 Ω per 5.5 cm
9	0.318	3.5	20 Ω per 7.5 cm
16	0.445	2.8	30 Ω per 9 cm
25	1.334	5.3	2 Ω per 11 cm
25	6.052	24.2	2 Ω per 7 cm

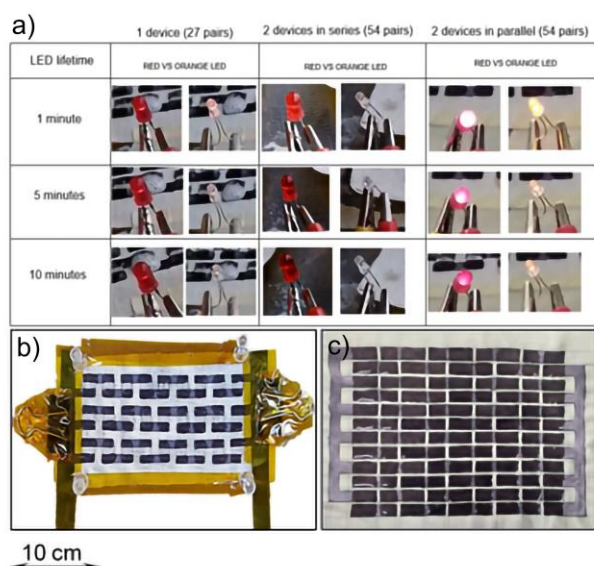


Figure S2 – Flat supercapacitors powering LEDs (a) having 54 (b) and 108 (c) electrodes

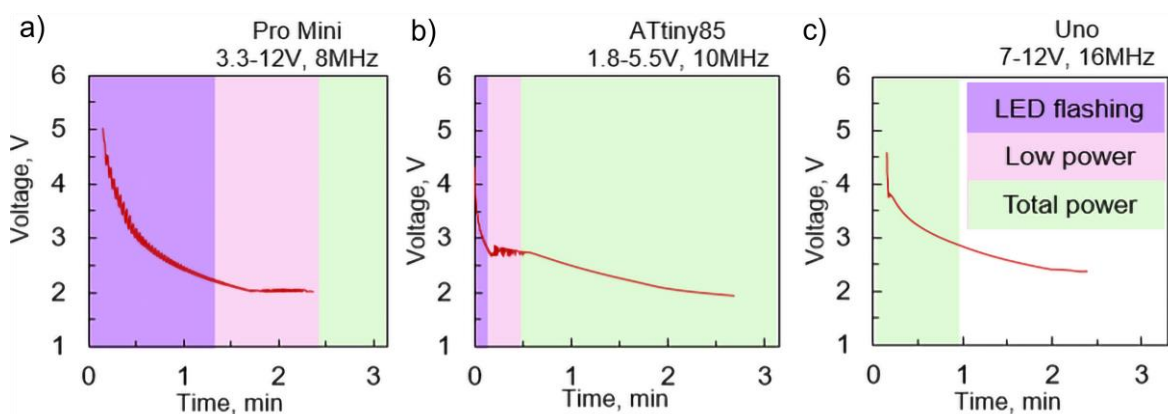


Figure S3 – Voltage discharge from supercapacitor into various common microcontrollers Pro Mini (a), ATtiny85 (b), Uno (c) captured with INA260

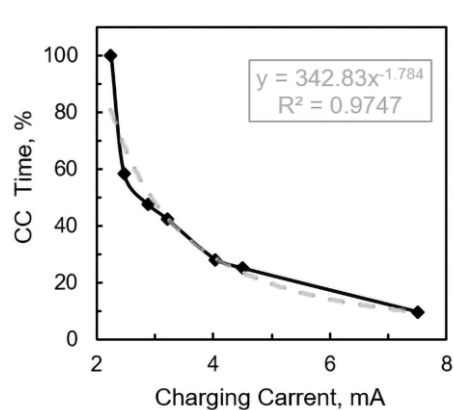


Figure S4 – Calibration curve to determine Galvanostatic Cycling with Potential limitation aka Constant Current (CC) % time with respect to applied current

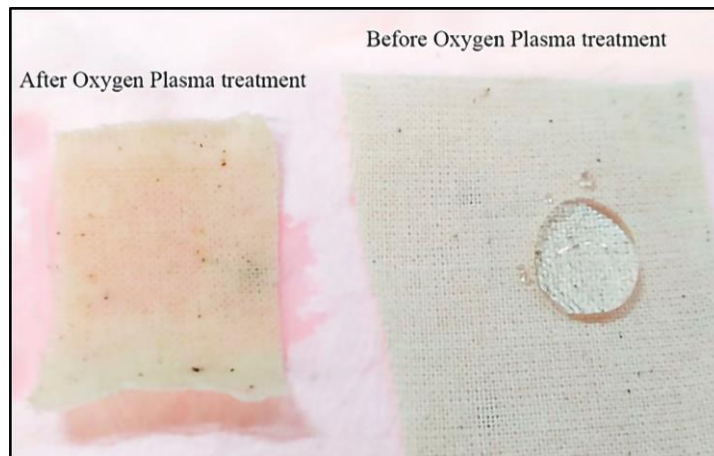


Figure S5 – Hydrophobic (Before Oxygen Plasma treatment) muslin cotton (Mybecca 100% Natural Cotton Muslin Woven Fabric Unbleached) used for drop casting of MXene electrodes

Table S4 – Conductivity of vacuum filtrated $\text{Ti}_3\text{C}_2\text{T}_x$ MXene film, including digital photographs of $\text{Ti}_3\text{C}_2\text{T}_x$ MXene film and its dispersion in water



Resistivity ($\Omega \square^{-1}$)	Thickness (cm)	Conductivity ($\text{S } \square^{-1}$)	Conductivity (S cm^{-1})	<Conductivity> (S cm^{-1})	$\text{Ti}_3\text{C}_2\text{T}_x$ film	$\text{Ti}_3\text{C}_2\text{T}_x$ in H_2O
0.2894	0.00040	3.46	8639	9213 \pm 8.7%		
0.2945	0.00039	3.40	8707			
0.2857	0.00034	3.50	10295			

Table S5 – Data on samples prepared for testing geometry configurations

Geometry	$\text{Ti}_3\text{C}_2\text{T}_x$ loading (mg)	#Coatings	R/electrode (Ω)	Separator Gap (cm)
'Stacked'	78	5	3	0.1 in Z direction
'Interdigit. #1' (I.1)	58	15	1	0.5
'Interdigit. #2' (I.2)	71	5	3	0.5
'2.Electrodes'	73	5	3	0.5
Geometry	Length (cm)	Width (cm)	Footprint Area (cm^2)	
'Stacked'	2.45	2.45	6	
'Interdigit. #1' (I.1)	2.45	2.45	6	
'Interdigit. #2' (I.2)	5.5	3.5	19.3	
'2.Electrodes'	5.5	2.5	13.8	
Geometry	Electrode #1 (cm^2)	Electrode #2 (cm^2)	Active Area (cm^2)	
'Stacked'	$2.45^2 = 6$	$2.45^2 = 6$	12	
'Interdigit. #1' (I.1)	$2 \cdot 0.5 + 3 \cdot 1 \cdot 0.25 = 1.75$	$2 \cdot 0.5 + 3 \cdot 1 \cdot 0.25 = 1.75$	3.5	
'Interdigit. #2' (I.2)	$1 \cdot 4.5 + 3 \cdot 1 \cdot 0.25 = 6$	$1 \cdot 4.5 + 3 \cdot 1 \cdot 0.25 = 6$	12	
'2.Electrodes'	$2.45^2 = 6$	$2.45^2 = 6$	12	
Geometry	Total Length (cm)	Total Width (cm)	Total Area (cm^2)	
'Stacked'	2.45	2.45	2.6 = 12	
'Interdigit. #1' (I.1)	2.45	2.45	6	
'Interdigit. #2' (I.2)	5.5	3.5	19.3	
'2.Electrodes'	5.5	2.5	13.8	

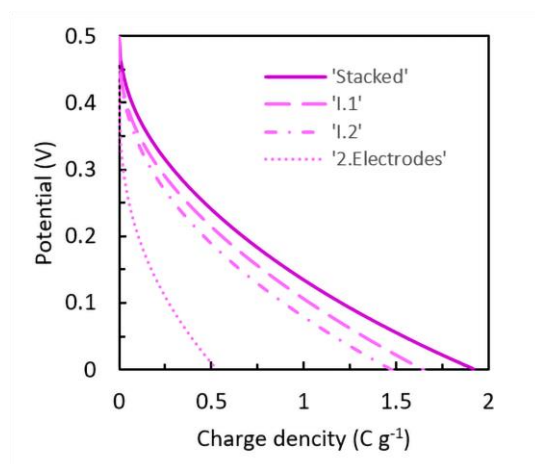


Figure S6 – Galvanostatic Cycling with Potential Limitation aka Constant Current (CC) discharge profiles of samples prepared for testing geometry configurations

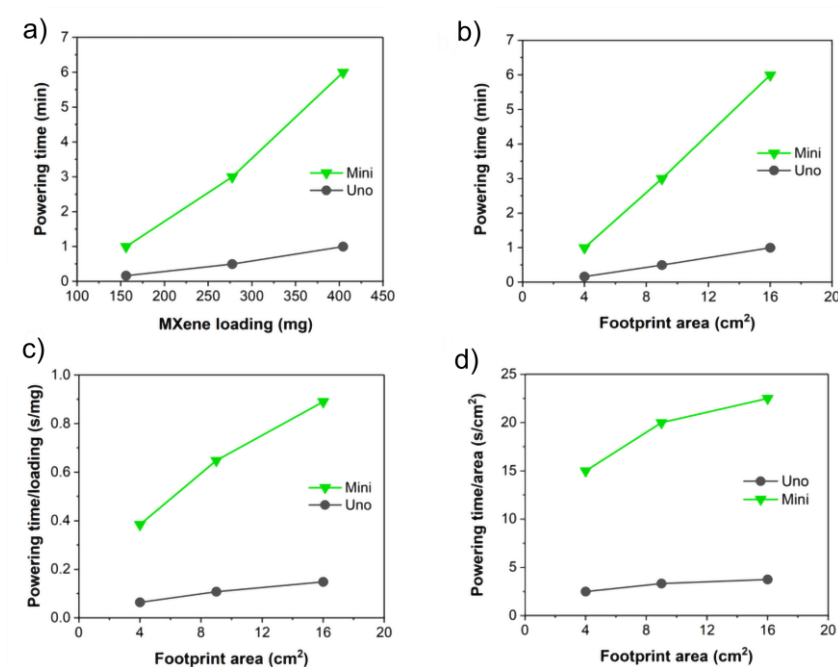


Figure S7 – Analysis of powering time of two different commercially available microcontrollers (Arduino Mini Pro 3.3 V and Arduino Uno). Power was provided via five cell devices with 4 cm², 9cm² and 16 cm². a-b) to demonstrate the amount of time the microcontrollers were powered as a function of total MXene loading and Footprint area. c-d) show normalized curves, and show no loss in efficiency with increased area and mass.

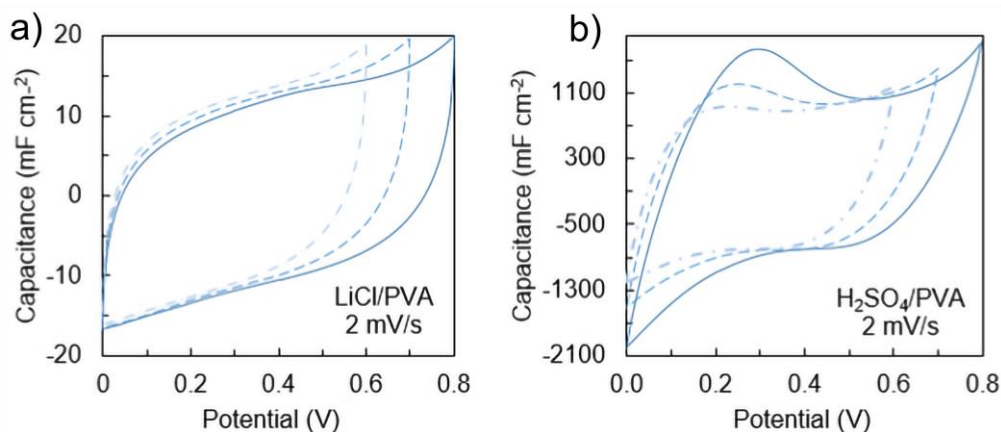


Figure S8 – Advantages of using LiCl/PVA (a) over H₂SO₄/PVA (b).

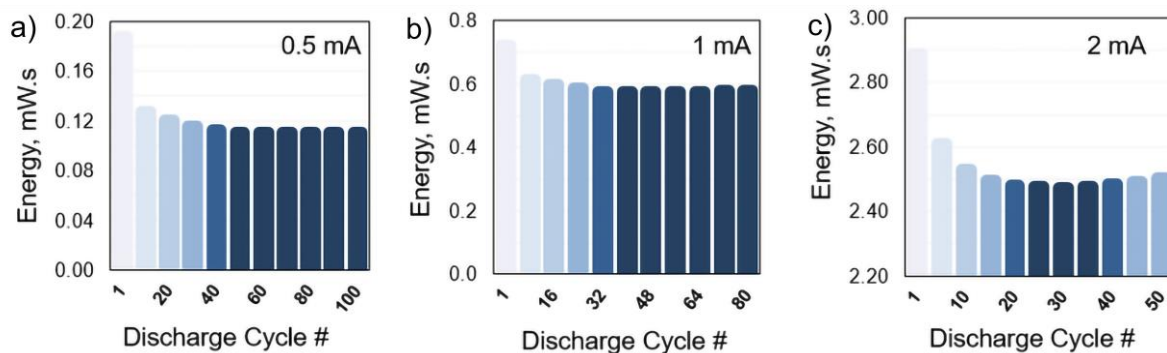


Figure S9 – Consistent energy provided upon repeated discharge power cycles of 0.5 mA (a), 1 mA (b) and 2 mA (c) (each discharge power cycle lasts for 10 sec and is followed by withdraw of 0.2 mA also referred as “standby” current)

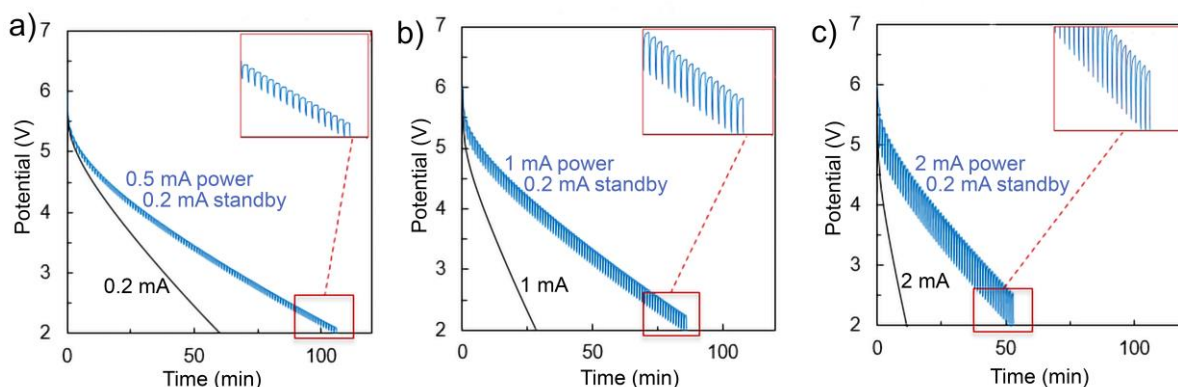


Figure S10 – Switching current increases performance of 25 cm² footprint area supercapacitor with 5.34 mg cm⁻² mass loading while having 0.5 mA (a), 1 mA (b), 2 mA (c) power cycles

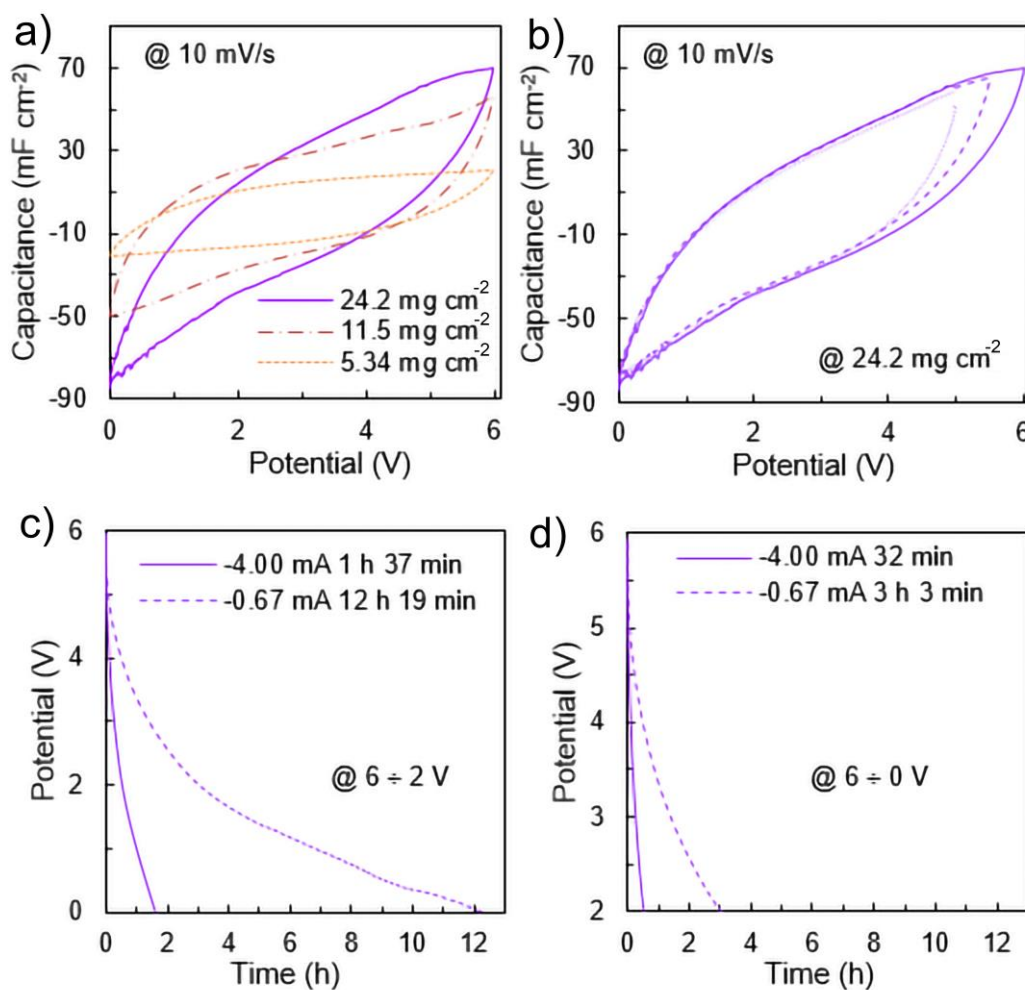


Figure S11 – Cyclic voltammetry at a scan rate of 10 mV/s with footprint area of 25 cm² and various MXene areal loading (a), Cyclic voltammetry with voltage window variation on a sample of 25 cm² and loading of 24.2 mg cm⁻² at a scan rate of 10 mV/s (b), Constant Current discharge profiles for the 25 cm² footprint area sample with loading of 24.2 mg cm⁻² at 6 V to 0 V (c) and 6 V to 2 V (d)

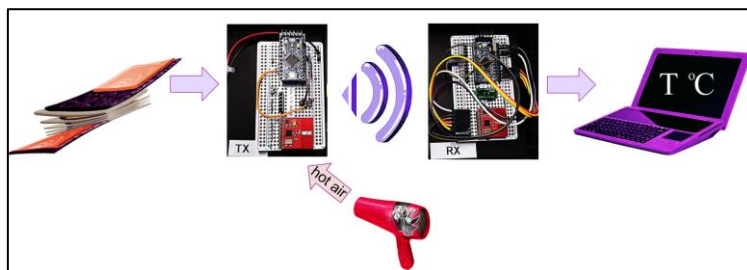


Figure S12 – Schematics of protocol for charging supercapacitor from power supply followed by using supercapacitor to power temperature sensor system

Table S6 – Current and voltage requirements for powering temperature sensor

Potential (ΔV)	Standby (mA)	Power cycle (mA)
6	0.67	1.3 \div 4.0
5	0.67	1.3 \div 4.0
4	0.67	1.3 \div 4.0
3.0 \div 2.3	1.25	3.5 \div 4.5
2.3 \div 2.1	3.6 \div 4.0	3.5 \div 4.5

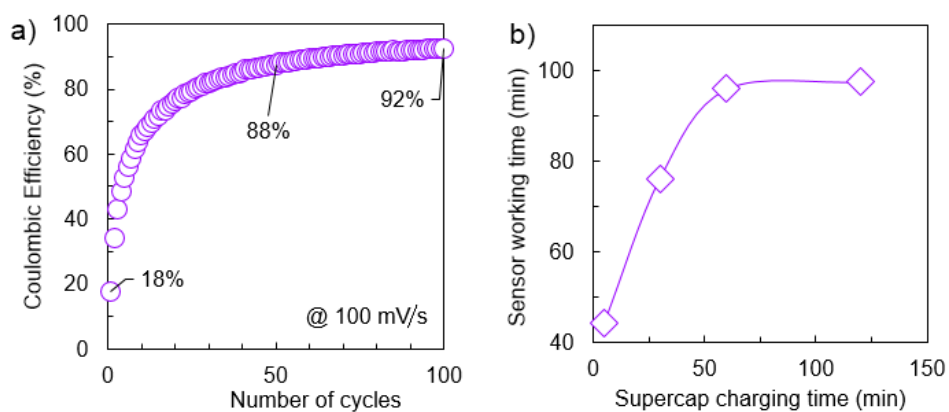


Figure S13 – Efficiency of 25 cm² footprint area supercapacitor 24.2 mg cm⁻² MXene loading after precycling at a scan rate of 100 mV/s (a) where charging up to 6 V and discharging cycles into temperature sensor system (b)

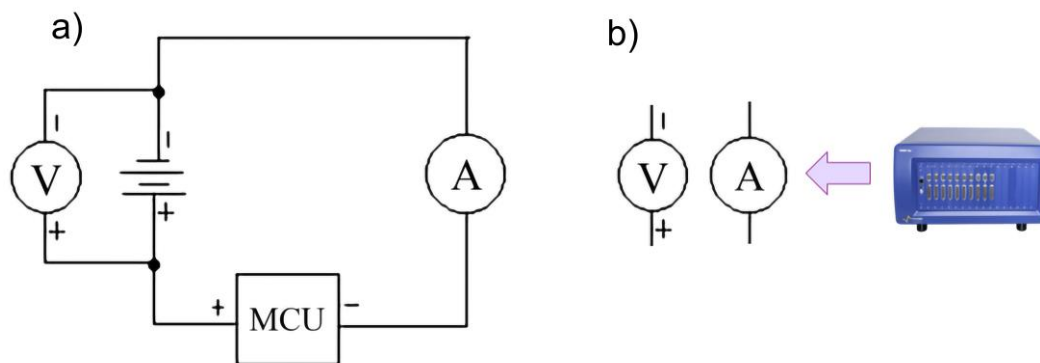


Figure S14 – Measurement configuration circuit schematics (a) and potentiostat functions within the circuit (b) to monitor current and voltage during withdraw from supercapacitor into temperature sensor system.

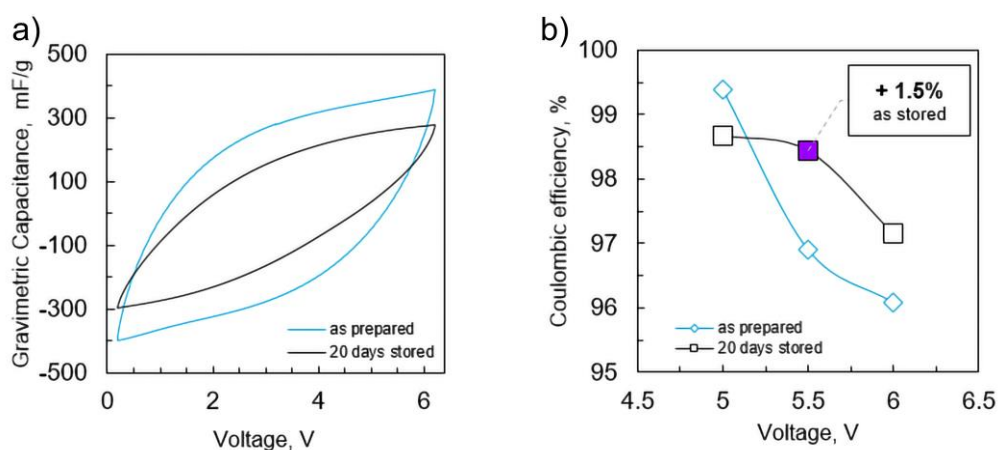


Figure S15 – Capacitance (a) and coulombic efficiency (b) after 20 days of storage

Detailed Experimental Protocols

MAX Synthesis. TiC (Titanium (IV) carbide powder, -325 mesh, 98%, purchased from Aldrich ® Chemistry), Ti (Titanium powder, -325 mesh, 99.5% (metals basis), purchased from Alfa Aesar) and Al (Aluminium powder, -325 mesh, 99.5% (metals basis), purchased from Alfa Aesar) powders were mixed manually in a TiC:Ti:Al = 2:1:1 mass ratio. After manual mixing obtained powder was ball milled. During ball milling, zirconia balls were used in the 2:1 mass ratio of zirconia balls (5 mm Spherical Premium Yttria Stabilized Zirconia YSZ Milling Media, purchased from MSE Supplies) to powder mixture. The ball milling was maintained for 18 hours at 70 rpm. The ball milled powder mixture was left to cool down overnight. The mixture was placed into an alumina crucible. The crucible was covered with graphite foil (Graphite foil, 0.254 mm (0.01 in) thick, 99.8% (metals basis), purchased from Alfa Aesar). A MTI GSL-1700X tube furnace was used to sinter the powder mixture. Sintering was maintained under the following conditions: heating/cooling rate – 3 °C/min, sintering temperature - 1380 °C, sintering time - 2 hours. Sintered MAX precursor was milled using a Baron ® CNC Mill. The milled MAX powder was HCl washed to reduce intermetallic impurities. For HCl washing, hydrochloric acid (Certified ACS Plus, 36.5 to 38.0%, Fisher Chemical™, purchased from Fisher Scientific) was diluted in deionized (DI) water from 12 M initial concentration down to 9 M concentration. The 0.5 L of diluted HCl was sufficient for washing approximately 50 grams of milled MAX powder. The washing was maintained overnight (typically, until gas evolution from the solution stopped). The solution was neutralized via vacuum filtration using DI water followed by drying MAX in an Across AccuTemp vacuum oven for 6 hours at 80 °C. Dried Al- Ti₃AlC₂ MAX powder was sieved through -400 mesh (38 µm) particle sieve.

Ti₃C₂T_x MXene Synthesis. First, the etching solution needs to be prepared. 6 mL of DI water is put into a high temperature resistant plastic bottle. A magnetic stir bar with an appropriate length, which is roughly equal to the diameter of the bottle, is put into the bottle. Then, 12 mL of Hydrochloric acid is added (Hydrochloric Acid, Certified ACS Plus, 36.5 to 38.0%, Fisher Chemical™, purchased from Fisher Scientific). After that, 2 mL of Hydrofluoric acid is added at once (Hydrofluoric acid, ACS reagent, 48-51% solution in water, purchased from Acros Organics). After the etching solution is ready, the bottle is put into a mineral oil bath, on a magnetic hot plate. A thermocouple is inserted into the mineral oil bath. The stirring is set to 100 rpm. Then, 1 gram of highly stoichiometric Ti₃AlC₂ MAX phase was added gradually. Once all MAX powder is added, the stirring is increased to 300 rpm and the temperature is set to 35 °C. It is necessary to wear a protective face shield, as well as protective acid resistant gloves and apron when handling hydrofluoric acid. The etching is done over 24 hours. The cover of the bottle is left loose to prevent both evaporation of etching solution and to allow space for gas release. After etching, washing is performed at 5,000 rcf (3,500 rpm) for 5 minutes using 300 mL DI water per cycle in a low-speed centrifuge from Thomas Scientific. 6-10 cycles are required to get down to neutral pH. Protective clothes are to be removed after pH reaches 5. Washed multi-layered MXene is then mixed with 50 mL DI water and 1.1 gram of anhydrous LiCl (Lithium Chloride, anhydrous, 99%, -20 mesh, purchased from Alfa Aesar). The intercalation is set overnight at 300 rpm and 35 °C. After intercalation, delamination is

performed at 5,000 rcf (3,500 rpm) in low-speed centrifuge from Thomas Scientific for 45 minutes using 300 mL DI water per cycle to release MXene flakes. Supernatant is collected. Sediment should be re-dispersed in DI water (via shaking the centrifuge bottle) and collecting cycles are repeated. The number of cycles can be as high as required until MXene is still released (supernatant has dark greenish color). Attention should be paid in order not to mix sediment with the supernatant that is to be collected (avoid shaking of the centrifuge bottle upon collecting supernatant). Supernatant that was collected during multiple cycles can be further concentrated in a high-speed centrifuge such as a Hermle Z446 by applying 15,000 rcf (10,000 rpm) for 5 minutes per cycle. Al-Ti₃AlC₂ MAX and Ti₃C₂T_x synthesis can be scaled up proportionally

Ti₃C₂T_x MXene Flakes Size Selection. After probe sonication the flakes size was examined via Dynamic Light Scattering (DLS) using Zetasizer Nano ZS, Malvern Panalytical, until the target flakes size is achieved. In order to achieve consistent flake size reduction, the probe sonicator tip should be immersed to the same depth batch to batch. The vessel with MXene was cooled either with a cooling pump or with an ice bath during probe sonication to prevent oxidation of MXene.

Gel Electrolyte Preparation. Upon LiCl and DI water mixing, since the reaction is exothermal, the heat is released, and the mixture is left to cool down to room temperature. After solution has cooled, a magnetic stir bar was placed in the solution. The solution with the magnetic stir bar was placed on the hot plate with the level of the oil higher than that of the solution in the bottle. PVA should be added gradually into the vortex for redistribution of the PVA. After the hot plate mixing the obtained electrolyte should be left to cool overnight and visually checked to avoid impurities and bubbles.

Supercapacitor Device Fabrication. To fabricate the stacked textile supercapacitors, cotton fabric was cut into 6 equal pieces. Two pieces were used as top and bottom substrates for the top and bottom electrodes. Each of the other four pieces was bent and attached to double sided silicone covered Kapton (polyimide) insulator tape (Bertech Double Sided Kapton (Polyimide) Tape, 0.003 cm thick, 5 cm wide, silicone adhesive on both sides). For the four out of 6 cotton substrates the bending and attaching to Kapton (polyimide) insulator tape (Bertech Double Sided Kapton (Polyimide) Tape, 0.003 cm thick, 5 cm wide, silicone adhesive on both sides) was performed. The bending was performed in such a manner that from both sides of the Kapton (polyimide) there were square areas of cotton left to form a footprint and connection of the cotton path to the opposite side of the Kapton (polyimide) tape. Therefore, each piece of cotton formed a substrate for a pair of connected (at the bending area) fabric electrodes separated by the Kapton (polyimide) insulator to prevent electrical shortage. As the result, there was a total of 4 bent cotton substrates, one top electrode substrate and one bottom electrode substrate prepared. All cotton fabric substrates together with Kapton (polyimide) were measured to record pristine weight before the coating (Mettler Toledo ME54TE Analytical Balance). The MXene solution was drop casted onto the substrates to prepare the electrode pairs (total of 5 pairs in the stacked configuration having 10 electrodes). During drop-casting, each electrode pair was attached to a support to hang while air-drying. Top and bottom electrodes were covered only on one of the sides, since it was the only side that was acting as

an active electrode. Multiple coating cycles were applied (approximately 8 to 12 cycles for each electrode) to achieve the desired loading. The next coating cycle was applied after MXene deposition from the previous cycle had dried (in air for approximately 15 to 30 minutes). After all MXene coating cycles were finished coated substrates were measured again (Mettler Toledo ME54TE Analytical Balance) to record the increase in mass. The total mass increase was recalculated per each square centimeter of coated fabric and afterwards, the total mass loading per active surface area was calculated. The active surface area is the footprint area which was also the area covered with electrolyte.

Notes

In Figure S1 the standard characterization techniques were applied to demonstrate properties of $\text{Ti}_3\text{C}_2\text{T}_x$ MXene. The techniques are as follows: DLS to determine particles size before and after probe sonication (PS for 10 min), Z-Potential to determine stability of MXene dispersion in water, UV-Vis of MXene dispersion to determine that there was no oxidation present after PS, XRD of vacuum filtrated film to show the chemical composition of MXene and XRD of Carbon Ukraine (UA) Ti_3AlC_2 MAX precursor as reference and high Al- Ti_3AlC_2 MAX precursor used in this study. Z-potential signifies stability of the dispersion, the more negative Z-potential is, the more stable is dispersion, whereas we can see that PS insignificantly improves stability of MXene within the water dispersion. In terms of XRD analysis generally, we see a few differences between the reference Carbon Ukraine (UA) and High Al- Ti_3AlC_2 precursor MAX phases. Conducting Rietveld Refinement on the two MAX phases shows differences in the lattice parameters, for the High Al- Ti_3AlC_2 precursor MAX, it has an a (c) lattice parameter of 3.08069 Å (18.60585 Å), this is in contrast to the reference Carbon Ukraine (UA) MAX, which has an a (c) lattice parameter of 3.08046 Å (16.61417 Å). MAX phases have been previously shown to incorporate different M, A, or X elements into the lattice, which in turn leads to a quantifiable difference in the lattice parameters^{31,32}. The High Al- Ti_3AlC_2 precursor MAX phase used in this work is closer to the ideal phase stoichiometry. The Al flux acts as an oxygen scavenger during the reaction, which in turn leads to less Ti-defects. In contrast, Carbon Ukraine (UA) MAX incorporates oxygen into the Al layer, which in turn leads to a more defective $\text{Ti}_3\text{C}_2\text{T}_x$ MXene after the etching. This has been previously shown in terms of conductivity and stability³³. XRD patterns were collected on a Rigaku Smartlab operating at 40 kV and 30 mA with Cu K-alpha radiation, from 3-90 degrees, with a step scan of 0.01 degrees and holding time of 0.75 s. Rietveld Refinement was conducted using GSASII.

Parameters of the samples tested specifically areal mass loading and footprint area are shown in Table S2 and Table S3 . Footprint area is equal to surface of one electrode. Since devices represent 10 electrodes stacked one on top of another one, footprint area is also equal to the total area that the device takes on a garment. Footprint area was chosen to calculate energy density of the 25cm² device. Energy density, capacitance and power density were calculated from GCPL (Galvanostatic Cycling with Potential Limitation) on a 25 cm² footprint

area device using following equations: $Q = It$, $C = Q/\Delta V$, $E = \int QdV$; $P=E/t$. Charging method was CV (Constant Voltage) of 6 V for 60 min.

Additional geometries are possible as seen in Figure S2; for instance, 54 and 108 electrodes can be assembled as a flat system. These devices were able to power an LED for 10 minutes.

Based on geometry testing results, the stacked cell configuration was chosen as the primary design. To increase the voltage window, the final 25 cm² design was assembled from five cells connected in series stacked one on top of another (5.3 mg cm⁻² MXene loading). This design was used to test how the supercapacitor discharges into microcontrollers programmed to blink an LED. Texas Instruments' INA260 was used to record discharge profiles as shown in Figure S3.

In Figure S4 the data was recorded on the 25 cm² footprint sample with 5.3 mg cm⁻² loading after storage for 20 days. Charge testing requires complicated calibration, therefore charging with CV (constant voltage) is more convenient; moreover, it results in improved performance and higher discharge time.

In this work non-treated cotton substrate (Figure S5) was used for electrodes preparation.

In Table S4 the MXene film was weighed upon drying and the concentration of solution was determined thereafter to be 14 mg mL⁻¹. Four-point probe resistance measurements were used to determine conductivity of the film.

Performance of each configuration was investigated in Table S5, with results showing the 'Stacked' configuration outperforms 'Interdigitated' and '2.Electrodes' configuration. The data on devices for geometry configuration testing is shown in Table S5.

In Figure S6 the testing was performed at -0.5mA after 5 min charge at 0.5 V Constant Voltage.

In Figure S7 in fact we see a small increase in efficiency hypothesized to be due to a in resistance between electrodes due to the increase in cross sectional area associated with larger electrodes.

In Figure S8 no secondary oxidation peaks are observed for LiCl/PVA cyclic voltammetry plots in opposite to H₂SO₄/PVA. Test performed on knitted samples at a scan rate of 2 mV/s, with yarn loading of 0.6 mg cm⁻¹. Samples taken with 2 electrodes each 0.3 x 0.8 cm. 0.16 mL of electrolyte was used for each sample.

In Figure S9 the energy drop upon various current discharge stays consistent throughout testing using BioLogic Potentiostat which signifies that supercapacitor can provide significant energy to meet programmable microelectronics requirements. The data are recorded on 25 cm² footprint sample with 5.3 mg cm⁻² loading at a scan rate of 10 mV/s after 20 days of storage. Also, switching current significantly increases performance of the device (Figure S10).

In Figure S11 the electrochemical testing of device with highest loading at 25 cm² footprint area also shows better performance. The cyclic voltammetry shows that area within charge-discharge curve has increased significantly with increase of mass loading. Constant Current from 6 to 2 V signifies effective discharge time (within the voltage that is sufficient for powering temperature sensor system).

To validate the supercapacitor device performance, it was used to power a temperature sensor system (Figure S12). The temperature output was collected as set of data points over time. The temperature change was controlled by hot air flow. A supercapacitor that had been tested prior to the experiment was attached to a power supply and left to charge at 5.9 V for 60 min. The active and standby current for the temperature system varies with respect to operating voltage (Table S6). In Figure S13 there is no significant difference observed in supercapacitor performance after 1 h and 2 h charge (at 5.9 V). Therefore, 1 h was chosen as a charging time to test final performance.

In Figure S14 to measure the voltage and current input from the supercapacitor into the temperature sensor system, the BioLogic potentiostat was integrated into the electrical circuit. The temperature sensor system is labeled MCU (Microcontroller Unit). The supercapacitor is labeled as multi-cell power source.

In Figure S15 utilizing a vacuum seal for storage prevented device degradation and increased coulombic efficiency. The data are recorded on a 25 cm² footprint sample with 5.3 mg cm⁻² loading at a scan rate of 10 mV/s after storing for 20 days.

References

1. J. Wang, L. Dong, C. Xu, D. Ren, X. Ma and F. Kang, *ACS Appl Mater Interfaces*, 2018, **10**, 10851-10859.
2. Y. Wang, X. Wang, X. Li, X. Li, Y. Liu, Y. Bai, H. Xiao and G. Yuan, *Advanced Functional Materials*, 2021, **31**, 2008185.
3. S. Yong, J. Owen and S. Beeby, *Advanced Engineering Materials*, 2018, **20**, 1700860.
4. J. Yu, J. Zhou, P. Yao, J. Huang, W. Sun, C. Zhu and J. Xu, *Journal of Power Sources*, 2019, **440**, 227150.
5. D. Wu and W. Zhong, *Journal of Materials Chemistry A*, 2019, **7**, 5819-5830.
6. Z. Wang, S. Qin, S. Seyedin, J. Zhang, J. Wang, A. Levitt, N. Li, C. Haines, R. Ovalle-Robles, W. Lei, Y. Gogotsi, R. H. Baughman and J. M. Razal, *Small*, 2018, **14**, 1802225.
7. Y. Wang, X. Wang, X. Li, Y. Bai, H. Xiao, Y. Liu, R. Liu and G. Yuan, *Advanced Functional Materials*, 2019, **29**, 1900326.
8. L. Wang, S. Li, F. Huang, X. Yu, M. Liu and H. Zhang, *Journal of Power Sources*, 2019, **439**, 227103.
9. L. Li, M. Zhang, X. Zhang and Z. Zhang, *Journal of Power Sources*, 2017, **364**, 234-241.
10. M. Liu, Z. Cong, X. Pu, W. Guo, T. Liu, M. Li, Y. Zhang, W. Hu and Z. L. Wang, *Advanced Functional Materials*, 2019, **29**, 1806298.
11. Y.-J. Gu, W. Wen and J.-M. Wu, *Journal of Materials Chemistry A*, 2018, **6**, 21078-21086.
12. X. Li, R. Liu, C. Xu, Y. Bai, X. Zhou, Y. Wang and G. Yuan, *Advanced Functional Materials*, 2018, **28**, 1800064.
13. Z. Li, M. Li, Q. Fan, X. Qi, L. Qu and M. Tian, *ACS Appl Mater Interfaces*, 2021, **13**, 14778-14785.
14. X. Li, L. Yuan, R. Liu, H. He, J. Hao, Y. Lu, Y. Wang, G. Liang, G. Yuan and Z. Guo, *Advanced Energy Materials*, 2021, **11**, 2003010.
15. D. Zhu, M. Yan, R. Chen, Q. Liu, J. Liu, J. Yu, H. Zhang, M. Zhang, P. Liu, J. Li and J. Wang, *Chemical Engineering Journal*, 2019, **371**, 348-355.
16. H. Liu, Q. Liu, H. You, L. Zang, M. Chen and C. Yang, *Journal of Electroanalytical Chemistry*, 2021, **893**, 115332.
17. Q. Jiang, N. Kurra, M. Alhabeb, Y. Gogotsi and H. N. Alshareef, *Advanced Energy Materials*, 2018, **8**, 1703043.
18. J. Lim, D. S. Choi, G. Y. Lee, H. J. Lee, S. P. Sasikala, K. E. Lee, S. H. Kang and S. O. Kim, *ACS Applied Materials & Interfaces*, 2017, **9**, 41363-41370.
19. Y. Lin, H. Zhang, W. Deng, D. Zhang, N. Li, Q. Wu and C. He, *Journal of Power Sources*, 2018, **384**, 278-286.
20. F. Shao, N. Hu, Y. Su, L. Yao, B. Li, C. Zou, G. Li, C. Zhang, H. Li, Z. Yang and Y. Zhang, *Chemical Engineering Journal*, 2020, **392**, 123692.
21. W. Zhao, J. Peng, W. Wang, B. Jin, T. Chen, S. Liu, Q. Zhao and W. Huang, *Small*, 2019, **15**, 1901351.
22. X. Wang, H. Li, H. Li, S. Lin, W. Ding, X. Zhu, Z. Sheng, H. Wang, X. Zhu and Y. Sun, *Advanced Functional Materials*, 2020, **30**, 0190302.
23. M. Barakzahi, M. Montazer, F. Sharif, T. Norby and A. Chatzitakis, *Electrochimica Acta*, 2019, **305**, 187-196.
24. H. Lee, G. Jung, K. Keum, J. W. Kim, H. Jeong, Y. H. Lee, D. S. Kim and J. S. Ha, *Advanced Functional Materials*, 2021, **31**, 2106491.
25. H. Hu, Z. Bai, B. Niu, M. Wu and T. Hua, *Journal of Materials Chemistry A*, 2018, **6**, 14876-14884.
26. J. Noh, C.-M. Yoon, Y. K. Kim and J. Jang, *Carbon*, 2017, **116**, 470-478.
27. P. Sun, R. Lin, Z. Wang, M. Qiu, Z. Chai, B. Zhang, H. Meng, S. Tan, C. Zhao and W. Mai, *Nano Energy*, 2017, **31**, 432-440.
28. Y. Yue, N. Liu, Y. Ma, S. Wang, W. Liu, C. Luo, H. Zhang, F. Cheng, J. Rao, X. Hu, J. Su and Y. Gao, *ACS Nano*, 2018, **12**, 4224-4232.
29. W. Shao, M. Tebyetekerwa, I. Marriam, W. Li, Y. Wu, S. Peng, S. Ramakrishna, S. Yang and M. Zhu, *Journal of Power Sources*, 2018, **396**, 683-690.
30. Q. Huang, D. Wang, H. Hu, J. Shang, J. Chang, C. Xie, Y. Yang, X. Lepró, R. H. Baughman and Z. Zheng, *Advanced Functional Materials*, 2020, **30**, 1910541.
31. M. Sokol, V. Natu, S. Kota and M. W. Barsoum, *Trends in Chemistry*, 2019, **1**, 210-223.
32. M. Han, K. Maleski, C. E. Shuck, Y. Yang, J. T. Glazar, A. C. Foucher, K. Hantanasirisakul, A. Sarycheva, N. C. Frey and S. J. May, *Journal of the American Chemical Society*, 2020, **142**, 19110-19118.
33. T. S. Mathis, K. Maleski, A. Goad, A. Sarycheva, M. Anayee, A. C. Foucher, K. Hantanasirisakul, C. E. Shuck, E. A. Stach and Y. Gogotsi, *ACS nano*, 2021, **15**, 6420-6429.